ADVANCED MATERIALS
www.advmat.de

Multimodal-Driven Magnetic Microrobots with Enhanced Bactericidal Activity for Biofilm Eradication and Removal from Titanium Mesh

*Carmen C. Mayorga-Martinez, Jaroslav Zelenka, Karel Klima, Michaela Kubanova, Tomas Ruml, and Martin Pumera**

Modern micro/nanorobots can perform multiple tasks for biomedical and environmental applications. Particularly, magnetic microrobots can be completely controlled by a rotating magnetic field and their motion powered and controlled without the use of toxic fuels, which makes them most promising for biomedical application. Moreover, they are able to form swarms, allowing them to perform specific tasks at a larger scale than a single microrobot. In this work, they developed magnetic microrobots composed of halloysite nanotubes as backbone and iron oxide (Fe_3O_4) nanoparticles as magnetic material allowing magnetic propulsion and covered these with polyethylenimine to load ampicillin and prevent the microrobots from disassembling. These microrobots exhibit multimodal motion as single robots as well as in swarms. In addition, they can transform from tumbling to spinning motion and vice-versa, and when in swarm mode they can change their motion from vortex to ribbon and back again. Finally, the vortex motion mode is used to penetrate and disrupt the extracellular matrix of *Staphylococcus aureus* biofilm colonized on titanium mesh used for bone restoration, which improves the effect of the antibiotic's activity. Such magnetic microrobots for biofilm removal from medical implants could reduce implant rejection and improve patients' well-being.

1. Introduction

Micro- and nanorobots are actively moving forms of matter that have found their way to biomedical applications.[1–7] Micro/nanomotors have been recently employed as tools for the eradication and removal of bacterial biofilms.[8–17] To achieve biofilm eradication, different strategies have been employed, such as reactive oxygen species generation through highly efficient (photo)catalysts used in light or magnetic-driven robots.[10,12] In addition, biorobots mechanically disrupt bacterial biofilms[14] or more specific peptide interactions driven by catalytic micromotors.[15] However, for biomedical application and for biofilm removal in a real-world setting, robots powered by a rotating magnetic field offer the advantage of biocompatibility of the motion mechanism and the capability to generate strong mechanical forces that can mechanically disrupt biofilm.[8,10–12] These robots have been used to remove and eradicate biofilms from indwelling

C. C. Mayorga-Martinez, M. Pumera
Center for Advanced Functional Nanorobots
Department of Inorganic Chemistry
University of Chemistry and Technology Prague
Technicka 5, Prague 166 28, Czech Republic
E-mail: martin.pumera@ceitec.vutbr.cz

J. Zelenka, M. Kubanova, T. Ruml
Department of Biochemistry and Microbiology
University of Chemistry and Technology Prague
Technicka 5, Prague 166 28, Czech Republic

K. Klima
Department of Stomatology – Maxillofacial Surgery
General Teaching Hospital and First Faculty of Medicine
Charles University
Prague 12808, Czech Republic

M. Pumera
Faculty of Electrical Engineering and
Computer Science
VSB - Technical University of Ostrava
17. listopadu 2172/15, Ostrava 70800, Czech Republic

M. Pumera
Department of Chemical and Biomolecular Engineering
Yonsei University
50 Yonsei-ro, Seodaemun-gu, Seoul 03722, South Korea

M. Pumera
Department of Medical Research
China Medical University Hospital
China Medical University
No. 91 Hsueh-Shih Road, Taichung 40402, Taiwan

The ORCID identification number(s) for the author(s) of this article can be found under https://doi.org/10.1002/adma.202300191

DOI: 10.1002/adma.202300191

medical devices such as dental implants and stents as well as tubing for medical equipment and tympanostomy tubing.[9–12,14]

Although antibiotic therapy remains the most common treatment modality for bacterial infections due to its established safety, efficiency, and specificity,[18,19] significant research efforts are still required to avoid the use of antibiotics for removing medical device biofilm. Another reason is the logistics developed for mass production and distribution of antibiotics worldwide.[20] In this sense, improving the antibacterial activity of antibiotics using miniaturized robots would be a better strategy to eradicate bacterial biofilms as many stages of production and massification for use in real applications are already optimized.

Reconstructive facial surgery is used to restore facial injuries and deformities and to restore normal function and appearance. The reconstruction of facial bones can be facilitated by the use of titanium meshes. Biomedical device-associated infections (BAIs) are the most common cause of treatment failure. *Staphylococcus aureus* (*S. aureus*) is the main cause of BAIs.[21,22]

Bacterial biofilm can lead to the loss of an expensive implant.

In this context, it can be considered that there are two strategies that can be used to avoid titanium mesh failure. The first is surface modification of the titanium mesh through an antibacterial drug coating or drug adsorption to develop drug-eluting titanium implants.[23] However, these strategies have some limitations such as low mechanical stability of drug-coated film as well as damage during insertion. In addition, in the case that the coated drug is an antibiotic, the risk of bacterial resistance increases due to inefficient drug delivery due to rapid and sudden bacterial colonization of the implant. The second strategy is to treat the infection of the implant once bacteria have colonized it. The main advantage of this strategy is the possibility to control the dose of the drug. However, the treatment is either oral or intravenous and includes long-term treatment with several doses per day, bringing discomfort associated with the administration route. On the other hand, once the implant is inserted, adhesion of the bone cells prevents bacterial colonization and vice-versa. In this sense, it is very important to effectively treat the infected implant to ensure the rapid adhesion of bone cells. Indeed, an infected implant or mesh requires a follow-up surgical procedure for its removal, with higher costs of medical care regardless of the lower quality of life of patients. Antibiotics are used as therapy for infected titanium meshes.[24] The penetration of antibiotics into biofilm is difficult and is often a cause of failure in the treatment of BAIs. For these reasons, the development of miniaturized robots to improve the penetration of antibiotics into the biofilm is important.

Recently, we reported on the treatment of dental and maxillofacial implants infected with bacterial biofilms using photoactive microrobots by reactive oxygen species (ROS) generation.[12,25] The limitation of these photoactive microrobots to treat biofilm is that they use UV or blue light illumination. Long-term exposure to blue light and ultraviolet (UV) irradiation is harmful and can produce side effects to patients and surgeons. Blue light can promote human eye refractive development and can dysregulate the circadian rhythm as well as produce different degrees of corneal, crystal lens, and retinal damage.[26] Therefore, it is necessary to take appropriate protective measures when using blue light-related products, especially at night. Besides, UV light plays an important role in non-cancerous ocular pathologies such as cataracts, glaucoma, and age-related macular degeneration.[27] The exposure of UV light to skin also has undesirable effects. Excessive exposure to UV light increases health risks, including atrophy, pigmentary changes, wrinkling, and skin malignancies. Moreover, UV radiation is classified as a "complete carcinogen" as it is both a tumor initiator and a tumor promoter.[28] In our previous works, we probe that maxillofacial and dental implants colonized with oral biofilm can be treated with photoactive microrobots. This is because the gums are covered by a keratinized epithelium and are very exposed for easy light penetration. On the other hand, these light sources do not penetrate to the deeper layers of subcutaneous tissue, thus making the use of these photoactive microrobots inefficient for the treatment of biofilm on implants for facial bone restoration. To avoid this problem, other strategies using microrobots have to be explored to kill and remove bacterial biofilm from implants.

Herein, we have addressed these challenges by developing magnetic microrobots prepared through the bottom-up controlled assembly of multiple nanometer-sized components, such as halloysite nanotubes (HNTs), iron oxide (Fe_3O_4) nanoparticles, and polyethylenimine (PEI), which is used to load the broad-spectrum antibiotic ampicillin (Amp). In this design, the HNTs in the microrobot backbone and the Fe_3O_4 nanoparticles mediate the microrobots' magnetic actuation. Magnetic microrobots based on HNTs and Fe_3O_4 nanoparticles were subsequently covered with high-molecular weight PEI in order to allow the antibiotic coating (see left and bottom side panel, **Scheme 1**). In addition, PEI works as a β-lactam potentiator to enhance the antibacterial activity of ampicillin.[29] The resulted magnetic microrobots exhibited the multimodal motion of single microrobots. Moreover, their swarming behavior could be transformed from one motion mode to another (top panel, Scheme 1). Finally, the multimodal movement presented by these magnetic microrobots was used to transport the drug to the targeted biofilm in order to penetrate the complex and sticky matrix of biofilm, and almost completely remove the biofilm from the titanium mesh (see right panel, Scheme 1). The results obtained in this work show the interaction of the bacterial biofilm with microscale magnetic micromotors. Such interaction utilizes their different modes of propulsion generated by a rotating magnetic field to treat efficiently highly dangerous bacterial biofilms. Such an achievement would have an important impact in reconstructive facial surgery that uses costly medical devices like titanium mesh.

2. Results and Discussion

Magnetic microrobots, designated HNT-Fe_3O_4@PEI/Amp, were prepared by the bottom-up controlled assembly of each nanocomponent. First, halloysite nanotubes (HNTs or microrobot skeleton) were attached to Fe_3O_4 (microrobot magnetic actuator) to obtain the HNT-Fe_3O_4 composite by electrostatic interactions. Then, HNT-Fe_3O_4 was covered with PEI to obtain HNT-Fe_3O_4@PEI. Finally, Amp was attached on the magnetic microrobots (see Scheme 1). The obtained magnetic microrobots were systematically characterized using transmission electron microscopy (TEM), high-resolution TEM (HR-TEM), selective area diffraction (SAED), and energy-dispersive X-ray spectroscopy (TEM–EDX) as well as Z-potential and thermogravimetric analysis (TGA).

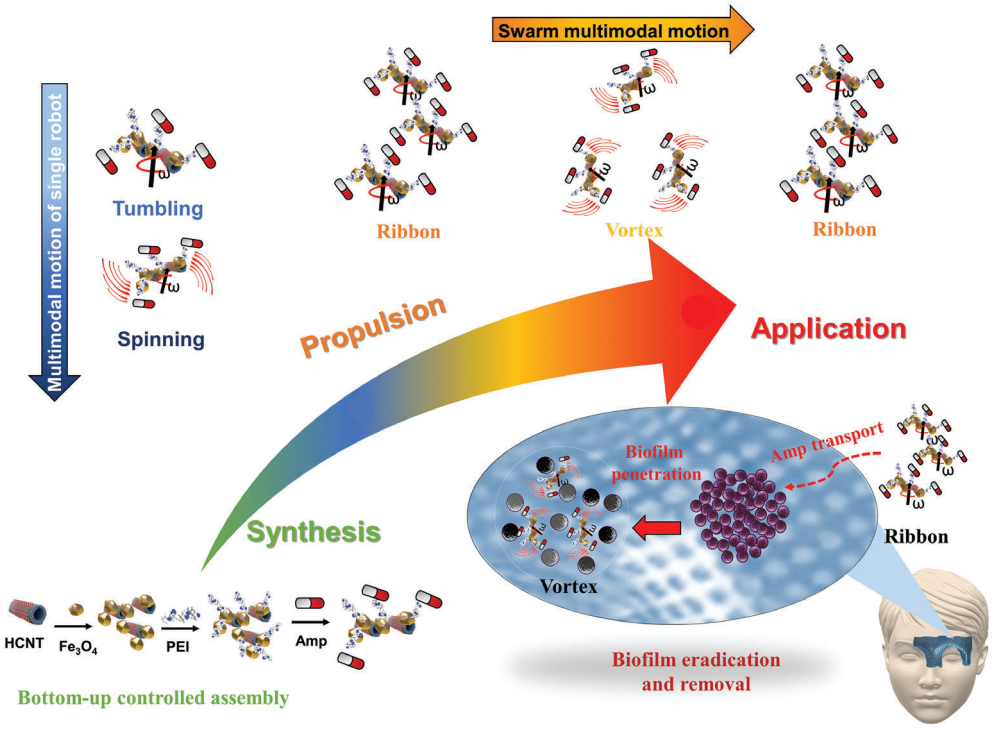

Scheme 1. Schematic representation of fabrication, motion ability, and antibacterial activity of HNT-Fe_3O_4@PEI/Amp microrobots. Synthesis: bottom-up controlled assembly of magnetic microrobots based on halloysite nanotubes (HNTs), Fe_3O_4 nanoparticles, polyethylenimine (PEI), and ampicillin (Amp). Propulsion: multimodal motion of single microrobot and swarm motion, and their transformation. Application: eradication and removal of *S. aureus* biofilm colonized on titanium mesh used for bone restorations.

TEM images obtained from pristine Fe_3O_4 and HNTs are represented in **Figure 1**A,B, respectively. Fe_3O_4 particles show uniform shape and size distribution with a length of ≈200 nm while HNTs show uniform tubular shape with a length of ≈400 nm. Moreover, HR-TEM and SAED demonstrated high crystallinity of both materials. After overnight the incubation of Fe_3O_4 and HNTs, and cleaning using an external magnet, TEM, HR-TEM, and SAED were performed. Images of the resulting material presented in Figure 1C clearly demonstrate the presence of both materials (HNTs and Fe_3O_4). Finally, Figure 1D shows the Fe_3O_4-HNT covered with a thin layer of PEI.

EDX elemental mapping from TEM images of each component of the bottom-up controlled assembly of HNT-Fe_3O_4@PEI magnetic nanorobots was performed. **Figure 2**A shows the elemental mapping EDX of pristine Fe_3O_4, demonstrating the presence of Fe and O. Moreover, elemental Si, Al, and O are observed in the EDX elemental mapping of HNT (Figure 2B). When both materials (Fe_3O_4 and HNTs) are assembled, EDX elemental mapping revealed the presence of Fe, Si, Al, and O (see Figure 2C). Finally, in the sample of Fe_3O_4-HNT/PEI, EDX elemental mapping showed the presence of N, which corresponded to PEI, as well as Fe, Si, Al, and O, corresponding to Fe_3O_4 and HNTs (see Figure 2D).

To confirm the successful coating of PEI on Fe_3O_4-HNT surface, thermogravimetric analysis (TGA) was performed of Fe_3O_4 nanoparticles, Fe_3O_4-HNT, and Fe_3O_4-HNT/PEI samples. The TGA analysis is displayed in **Figure 3**A. The results showed variations of residual masses of the samples with changing temperature. The TGA profile of Fe_3O_4 did not show any weight loss (black line), but when Fe_3O_4 was attached to HNT, its TGA curve showed maximum weight loss at ≈350–520°C, corresponding with the dehydroxylation of structural aluminol groups present in HNTs (green line).[30] This is in good agreement with values of TGA obtained from HNTs (yellow line).[31] Finally, the TGA curve of Fe_3O_4-HNT/PEI showed weight loss of PEI[32] at ≈100–340°C and a weight loss of HNTs at ≈350–520°C (red line).

Furthermore, the successful fabrication of Fe_3O_4-HNT/PEI@Amp magnetic microrobots was monitored by Z-potential measurements (see Figure 3B). The attachment between Fe_3O_4 (positively charged)[33] and HNTs (negatively charged) was possible by electrostatic interaction in solution at pH 6. The resulted material, Fe_3O_4-HNT, showed a positive surface charge of 29.10 ± 1.19 mV; after Fe_3O_4-HNT was coated with PEI, the surface charge changed to more positive values (47.97 ± 1.34 mV). Finally, the surface charge of Fe_3O_4-HNT/PEI became less positive (24.42 ± 0.99 mV) when modified with Amp. The last step was possible due to the negative charge of Amp in solution at pH 7.4.[34] In addition, Amp loading on Fe_3O_4-HNT/PEI magnetic microrobots was quantified by mass spectroscopy (see Experimental Section). For 1 mg of Fe_3O_4-HNT/PEI magnetic microrobots, 1 mg of Amp was loaded.

Once the chemical and morphological structures of the magnetic Fe_3O_4-HNT/PEI@Amp microrobots were confirmed, their dynamics under a transversal magnetic field was investigated. We first studied the magnetic actuation of individual Fe_3O_4-HNT/PEI@Amp microrobots. **Figure 4**A (left panels) and

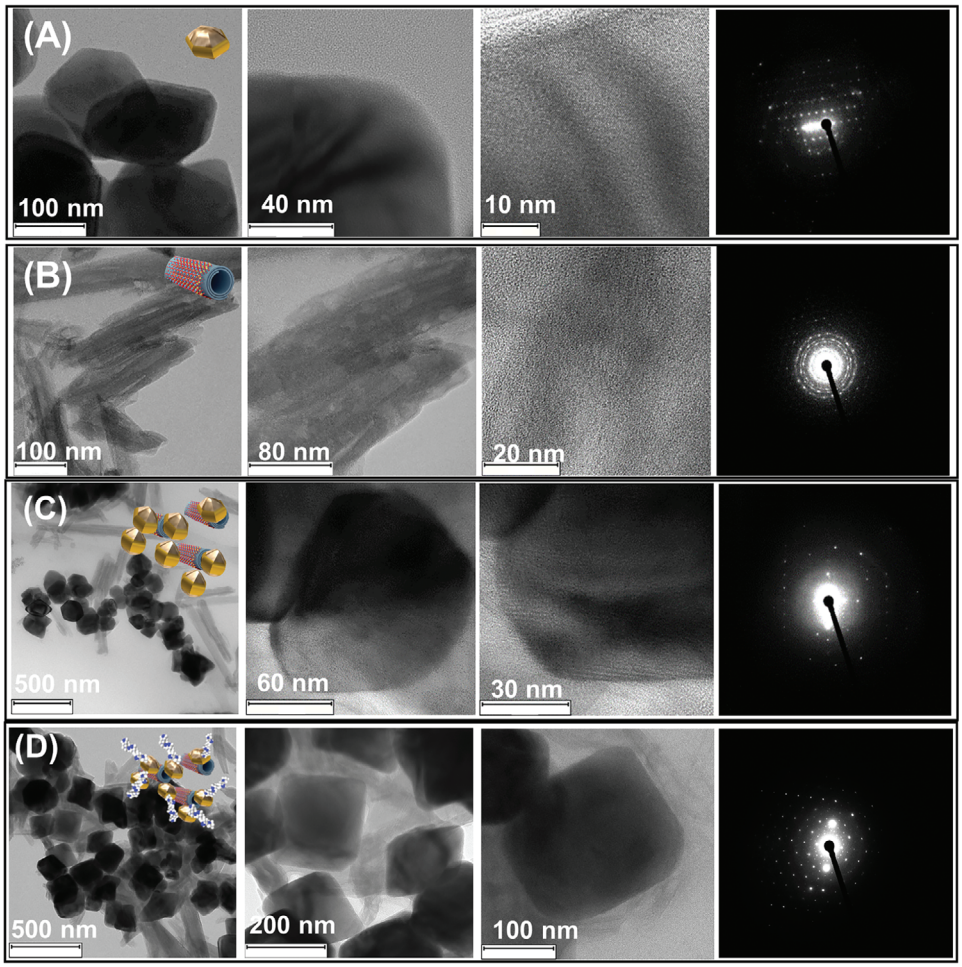

Figure 1. TEM images at different amplifications and SAED of each component during bottom-up controlled assembly of magnetic microrobots. A) Fe_3O_4 NPs and B) halloysite nanotubes (HNTs) were assembled to produce C) Fe_3O_4-HNT. Finally, polyethylenimine (PEI) was coated onto this structure, forming D) Fe_3O_4-HNT/PEI. Schematics of the individual steps are shown as insets.

Video S1 (Supporting Information) show that at low frequencies (0.3–2 Hz), microrobots exhibit a tumbling motion. However, at higher frequencies (4–10 Hz), the tumbling motion of individual Fe_3O_4-HNT/PEI@Amp microrobots looks like a high-speed micro-propeller (Figure 4A right panels and Video S2, Supporting Information). Moreover, by using a transversal rotating magnetic field, we have full directional control of the Fe_3O_4-HNT/PEI@Amp microrobots by changing the angle of the rotation plane on a two-dimensional surface (see Figure 4B and Video S3, Supporting Information).

In addition, the spinning motion generated by a programed clockwise circular rotation angle at different frequencies was evaluated (**Figure 5**A and Video S4, Supporting Information). Under this motion mode, the displacement of magnetic Fe_3O_4-HNT/PEI@Amp microrobots increases with an increase of frequency from 0.3 to 2 Hz; however, at higher frequencies the displacement gradually decreases. Finally, the multimodal motion combined tumbling and spinning of one Fe_3O_4-HNT/PEI@Amp microrobot at 1 Hz was evaluated. Figure 5B and Video S5 (Supporting Information) show the tracking line of a single Fe_3O_4-HNT/PEI@Amp microrobot that can easily switch from tumbling to spinning mode and back again to tumbling mode. Moreover, the microrobot is able to avoid an obstacle and return to its original path.

Previously, we developed a catalytic nanomotor based on halloysite nanotubes, where a thin layer of Pt covered halloysite nanotubes partially and the fuel was highly concentrated H_2O_2 (4%). This fuel at this concentration is highly toxic and not biocompatible at all. That is why these catalytic nanomotors were used for water cleaning and mercury detection. However, it was shown that halloysite nanotubes are a promising material for the "skeleton" of micro/nanomotors. In this work, we use the same body (halloysite nanotubes) for the microrobots and then attached Fe_3O_4 nanoparticles for their magnetic actuation.

The self-organization of micro-nanorobots in swarms gives them the ability to be synchronously maneuvered and to perform multiple tasks for which single micro/nanorobots are at risk of not achieving. Thus, a swarm of micro/nanomachines has the main advantages of greater effectiveness, robustness, and adaptability to multiple environments. In this way, the self-organization of magnetic Fe_3O_4-HNT/PEI@Amp microrobots in swarms was evaluated. Under a transversal rotating magnetic

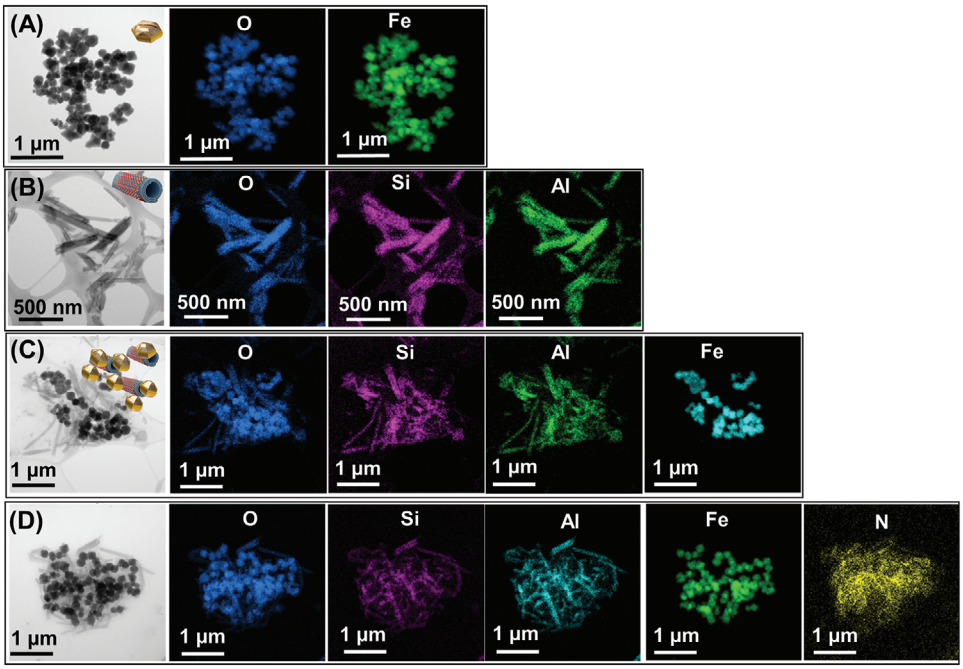

Figure 2. EDX elemental mapping from TEM images of each component of the bottom-up controlled assembly of magnetic nanorobots. A) Fe_3O_4 and (B) HNTs were assembled to produce (C) Fe_3O_4-HNT. Finally, D) polyethylenimine (PEI) was coated onto the Fe_3O_4-HNT surface, leading to the generation of Fe_3O_4-HNT/PEI. Schematics of the individual steps are shown as insets.

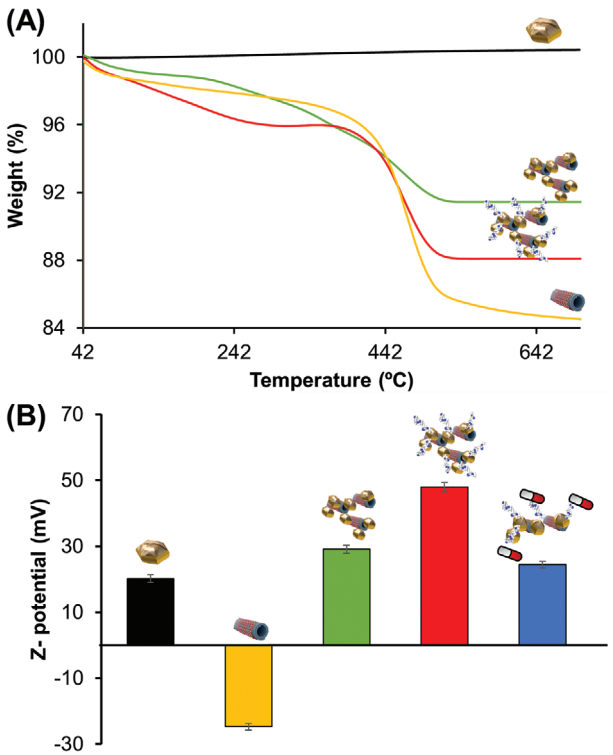

Figure 3. Thermogravimetric analysis (TGA) and zeta-potential measurements: (A) TGA of Fe_3O_4 (black line), Fe_3O_4-HNT (blue line), and Fe_3O_4-HNT/PEI (red line). (B) Z- potential of Fe_3O_4 (orange column), HNTs (yellow column), Fe_3O_4-HNT (green column), Fe_3O_4-HNT/PEI (blue column), and Fe_3O_4-HNT/PEI@Amp (red column).

field at high frequencies, magnetic Fe_3O_4-HNT/PEI@Amp microrobots showed tumbling motion. Moreover, easily two or more microrobots met and synchronized their motion in a ribbon swarm (see Videos S6 and S7, Supporting Information). Otherwise, when the Fe_3O_4-HNT/PEI@Amp microrobots moved under spinning mode, they generated the vortex swarm (see Video S8 and Video S9). In addition, we observed that the swarm of Fe_3O_4-HNT/PEI@Amp microrobots can be transformed from ribbon to vortex and conversely (see **Figure 6**, Videos S10 and S11, Supporting Information).

Staphylococcus aureus is a pathogen associated with the chronic biofilms that colonize implanted medical[24] devices such as titanium mesh used for bone restorations. Indeed, biofilms related to *S. aureus* are responsible for increased morbidity and mortality of patients with indwelling implants.[24] Biofilms are communities of microorganisms protected by a slimy extracellular polymeric substance. The bacterial biofilm contributes to microcolony formation and more complex architecture in 3D structures as well. The extracellular sticky matrix allows bacteria to survive in hostile environments.[24] The biofilm can be resistant to not only the host's immune system but also to antibiotics due to their inability to thoroughly penetrate this matrix structure. Moreover, when titanium mesh is colonized with a biofilm, treatment by antibiotics or surgical removal requires additional costs and increases patient morbidity and mortality. Our newly developed magnetic Fe_3O_4-HNT/PEI@AMP microrobots, when used as a swarm in ribbon mode, facilitated the transportation of a drug and delivered it to a targeted biofilm surface. However, the swarm in vortex mode allowed the magnetic microrobots to penetrate the biofilm's extracellular sticky matrix and subsequently disrupt and remove the matrix material.

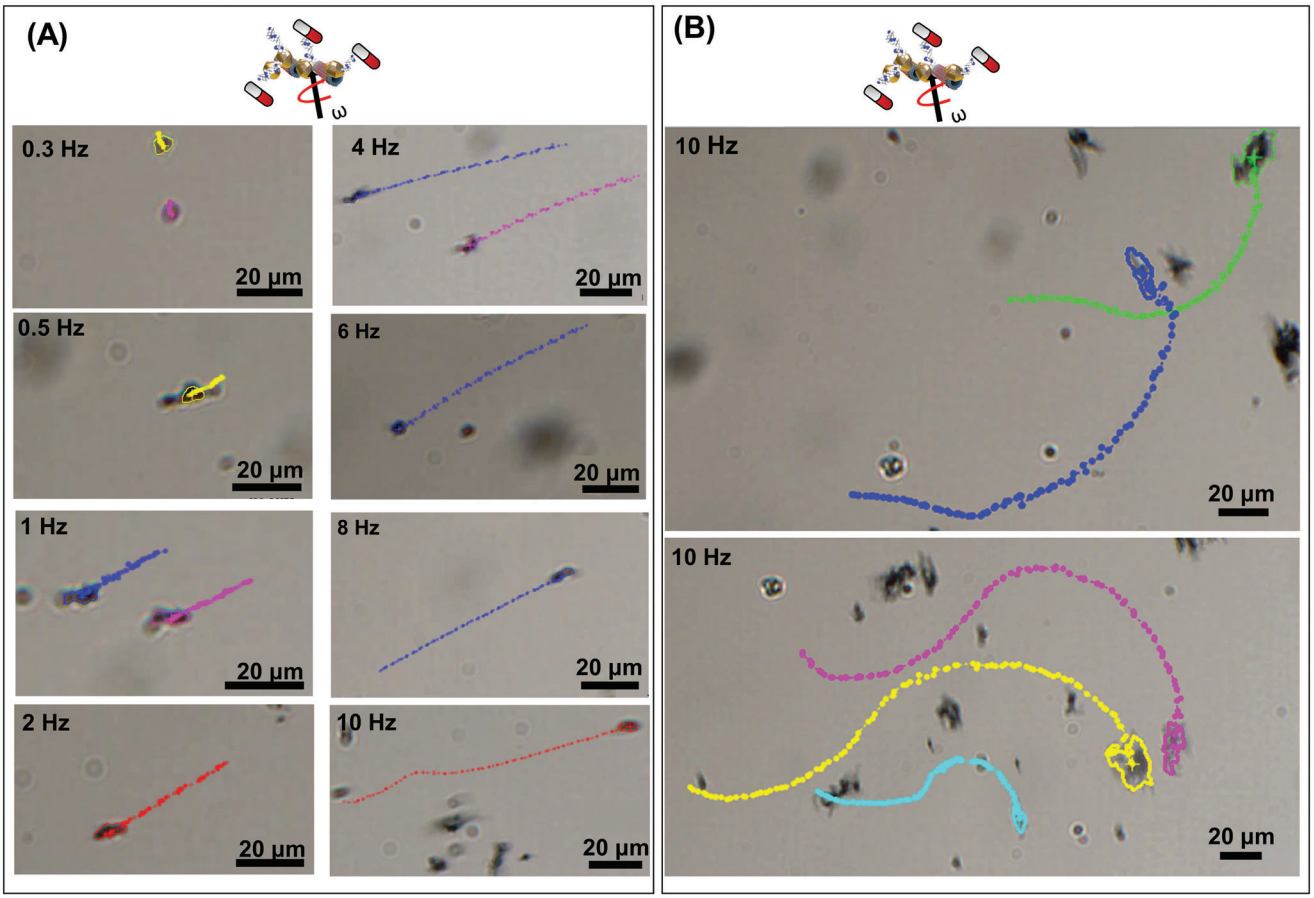

Figure 4. Fe_3O_4-HNT/PEI@Amp microrobot motion evaluation. Time-lapse optical microscopy images of tracking lines of (A) tumbling motions of individual magnetic Fe_3O_4-HNT/PEI@Amp microrobots. B) Direction control of tumbling motion of magnetic Fe_3O_4-HNT/PEI@Amp microrobots at 10 Hz.

To prove the capability of a swarm in ribbon mode to transport the antibiotic by Fe_3O_4-HNT/PEI@Amp magnetic microrobots, we introduced them in a glass capillary and recorded the result in Videos S12 and S13 (Supporting Information). Video S12 (Supporting Information) shows multiple ribbons formation and how the microrobots move along the glass tube. Video S13 (top panel) (Supporting Information) displays how swarm magnetic microrobots in ribbon mode can avoid obstacles and Video S13 (bottom panel) (Supporting Information) shows the merging of ribbons and their synchronization to move as one entity.

Video S14 (Supporting Information) shows the swarm motion of Fe_3O_4-HNT/PEI@Amp magnetic microrobots in vortex mode in media and the biofilm matrix; in both cases, the magnetic microrobots generated vortices in a similar way. In addition, we evaluated the interaction of magnetic Fe_3O_4-HNT/PEI@Amp microrobots with bacterial biofilm over time. A clear structural change in the extracellular sticky matrix of the biofilm was observed after 60 min (see bottom right panel of Video S15, Supporting Information). This observation indicates the penetration of magnetic Fe_3O_4-HNT/PEI@Amp microrobots inside the biofilm matrix. When shorter times are applied, the microrobots are not capable to fully penetrate the matrix of biofilm (see bottom left and top right panels of Video S15, Supporting Information). The 24 h period is the usual incubation time used to evaluate the antibacterial activity of antibiotics against biofilms.[35] In addition, antibiotic therapy requires several doses per day over several days. This applies also for penicillin-type antibiotics, including ampicillin, which inhibit the synthesis of the bacterial peptidoglycan component of the bacterial cell wall.[36] Therefore, to evaluate the antibacterial activity of magnetic microrobots, they were incubated with the treated biofilm for 24 h, which should be sufficient time for ampicillin to take its inhibitory effect.

Finally, magnetic actuation was applied to generate a swarm in vortex mode and videos at different times were recorded (Video S16, Supporting Information). Magnetic actuation conditions were 10 Hz, 5 mT, and 1 h under vortex motion mode. At 0 min, a change in the biofilm structure was observed that is probably due to bacteria killed by the ampicillin effect; after 60 min of magnetic actuation, biofilm disruption was observed clearly (bottom right panel of Video S16, Supporting Information). Lower time of magnetic actuation can also disrupt biofilm (see bottom left and top right panels of Video S16, Supporting Information). However, 60 min was allowed to ensure complete disruption of the biofilm.

To prove the biofilm eradication and disruption, LIVE/DEAD staining fluorescence microscopy was employed (**Figure 7**A). Untreated biofilm (Figure 7A) presented abundant live

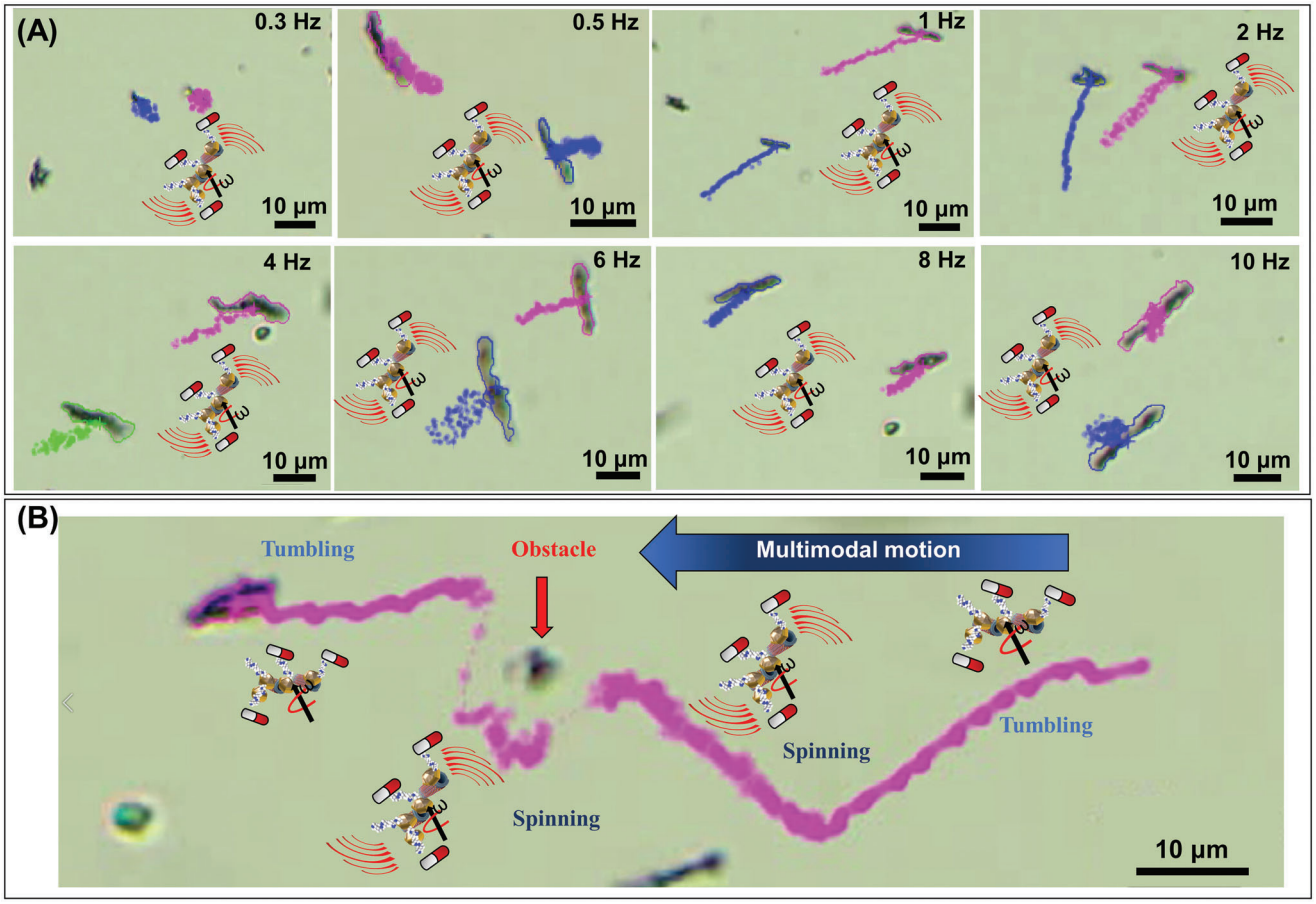

Figure 5. Motion of an individual Fe_3O_4-HNT/PEI@Amp microrobot. Time-lapse microscopy images of tracking lines. (A) Spinning motion of single magnetic Fe_3O_4-HNT/PEI@Amp microrobots at different frequencies. (B) Multimodal motion of individual magnetic Fe_3O_4-HNT/PEI@Amp microrobot from tumbling to spinning and from spinning to tumbling again at 1 Hz, and its ability to avoid an obstacle.

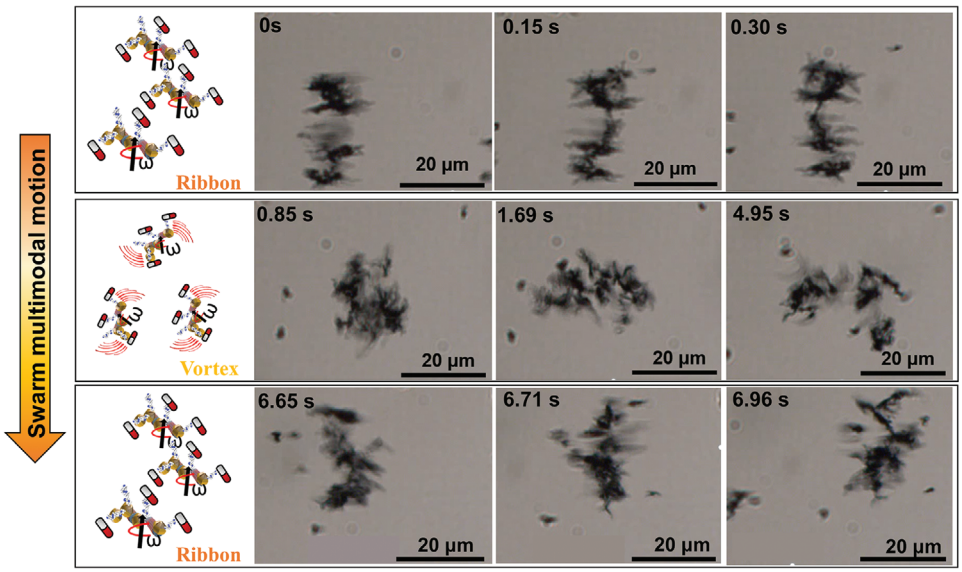

Figure 6. Swarm multimodal motion. Ribbon to vortex transformation and conversely of magnetic Fe_3O_4-HNT/PEI@Amp microrobots. Conditions: frequency 8 Hz; magnetic field intensity 5 mT.

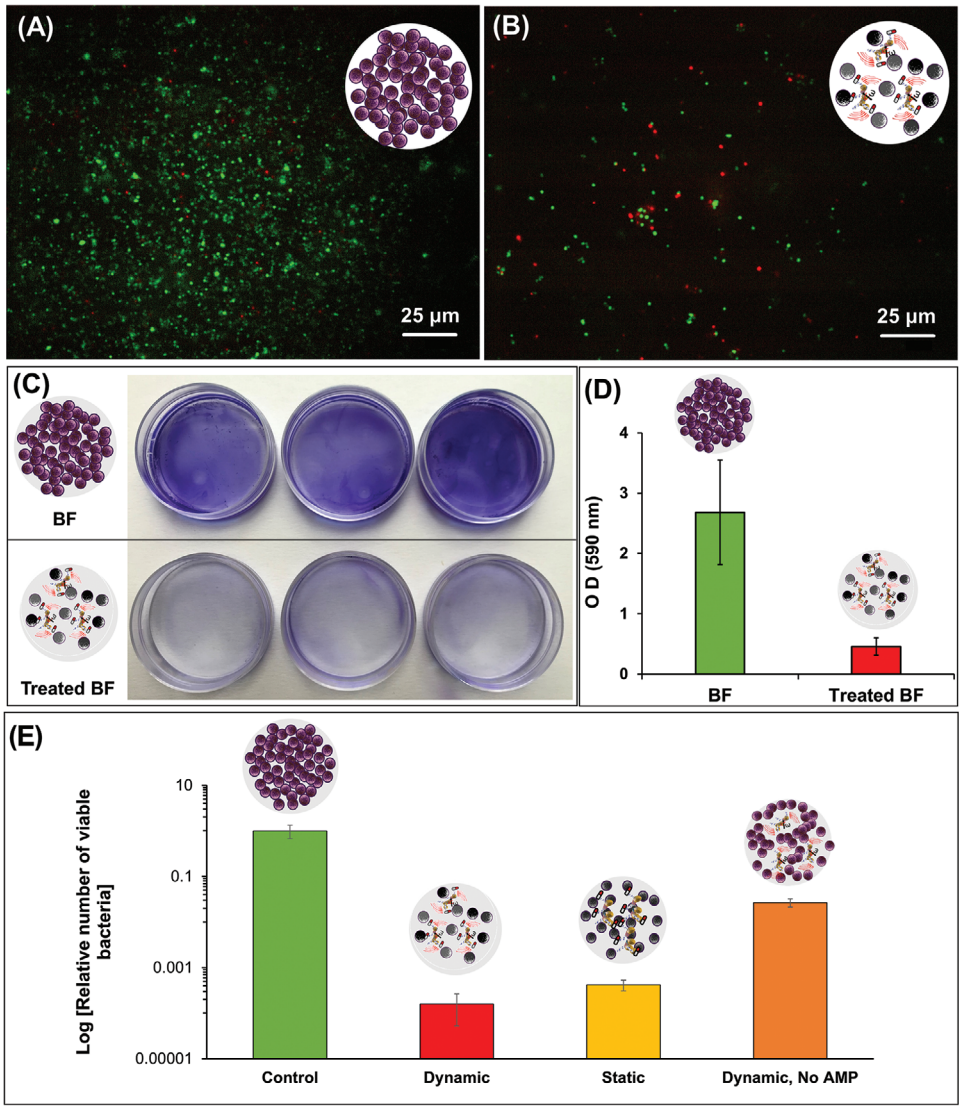

Figure 7. Antibacterial activity evaluation of Fe_3O_4-HNT/PEI@Amp magnetic microrobots on a flat surface (Petri dishes). (A) Bacterial viability visualization by fluorescence microscopy of LIVE/DEAD-stained biofilms of *S. aureus* untreated and (B) treated with Fe_3O_4-HNT/PEI@Amp magnetic microrobots. (C) Crystal violet staining of intact biofilm (top) and treated biofilm (bottom) and (D) absorbance measurement at 590 nm of crystal violet from untreated and treated biofilms dissolved in DMSO. (E) Relative numbers of viable bacteria of intact biofilm (green column) and treated biofilm (red column) with Fe_3O_4-HNT/PEI@Amp and magnetic actuation as well as the comparison with biofilm treated with Fe_3O_4-HNT/PEI@Amp in static (yellow columns) and dynamic Fe_3O_4-HNT/PEI microrobots without ampicillin (orange column). Values are the average of three independent measurements and data are displayed as mean ± SD.

bacteria (green spots), whereas biofilm treated with magnetic Fe_3O_4-HNT/PEI@Amp microrobots under magnetic actuation contained only a small number of bacteria and most of them were dead (see red spots in Figure 7B). In addition, the viability of bacteria surviving the treatment with magnetic Fe_3O_4-HNT/PEI@Amp microrobots under magnetic actuation was determined using crystal violet staining (Figure 7C,D) and the cultivation method (Figure 7E). Crystal violet staining is a gold standard methodology to evaluate the adherence of biofilm to flat surfaces. Digital photographs of crystal violet staining (Figure 7C top panel) show that intact biofilm is stained more intensely than the biofilm treated with Fe_3O_4-HNT/PEI@Amp microrobots (Figure 7C top panel). The quantification of biofilm adhesion was obtained by measuring the optical density (OD) of biofilms dissolved in DMSO at 590 nm. Figure 7D shows higher OD of intact biofilm compared to biofilm treated with Fe_3O4-HNT/PEI@Amp microrobots. In addition, SEM images showed morphological changes to the structure of *S. aureus* cells that occurred during treatment with the Fe_3O_4-HNT/PEI@Amp microrobots (see Figure S3, Supporting Information).

The results shown in Figure 7E demonstrate that the relative number of viable bacteria decreased by four orders of magnitude after treatment with magnetic Fe_3O_4-HNT/PEI@Amp microrobots and under magnetic (dynamic) actuation (see columns green and red). The results of the crystal violet staining and SEM analysis are in good agreement with the cultivation method.

However, the cultivation method is more sensitive for quantifying bacterial viability. Using a two-tailed *t*-test, a significant signal difference with $p = 0.006$ was observed ($\alpha = 0.05$, $n = 3$) between the intact biofilm and biofilm treated with dynamic Fe_3O_4-HNT/PEI@Amp microrobots. However, static Fe_3O_4-HNT/PEI@Amp microrobots decreased bacterial viability to a lesser extent (see yellow column). Nevertheless, they were statistically different with $p = 0.043$ ($\alpha = 0.05$, $n = 3$) when we applied the two-tailed *t*-test analysis to dynamic and static approaches. Finally, the ampicillin-free microrobots with only magnetic actuation decreased the bacterial viability only by two orders of magnitude (orange column). The relative viability of biofilm treated with Fe_3O_4-HNT/PEI@Amp microrobots was significantly different with $p = 0.001$ regarding Fe_3O_4-HNT/PEI microrobots using a two-tailed *t*-test ($\alpha = 0.05$, $n = 3$).

In addition, free ampicillin was used to treat the *S. aureus* biofilm in a control experiment (see Figure S1, Supporting Information). Interestingly, free ampicillin did not affect the biofilm resident bacteria viability, proving that the antibiotic must penetrate the biofilm matrix to kill them. The experimental groups comprising intact and ampicillin-treated biofilms were not statistically different with $p = 0.191$ ($\alpha = 0.05$, n = 3) based on a two-tailed *t*-test.

In addition, the absence of PEI, which acts as a β-lactam potentiator, is another factor decreasing ampicillin activity in this experiment.[37,38]

To evaluate the particles aggregation in artificial wound medium, we performed an additional experiment. In this experiment, instead of using pure Luria–Bertani (LB) medium to disperse the microrobots for the biofilm treatment, we combined it with Minimum Essential Medium Eagle used for tissue cell culture in proportion 1:1 (see Figure S2, Supporting Information). The results demonstrated that the medium where microrobots are dispersed slightly affects their performance to eradicate biofilms;, i.e., when the motors were dissolved in the pure LB medium, 99.98% of the biofilm was eradicated, whereas if the microrobots were dissolved in the mixed media, the biofilm was 99.1% eradicated. Moreover, the effects of the microrobots' motion under magnetic actuation were evaluated using different solutions that mimic the wound environment of a biological tissue (bovine serum, LB media, Minimum Essential Medium Eagle, and mixed media) (see Video S17, Supporting Information). As can be seen, the motion of Fe_3O_4-HNT/PEI@Amp microrobots was not affected and they were freely moving in all solutions tested.

Staphylococcus aureus infection is the major cause of titanium-based implant failure. The current treatment of these infections is the systemic delivery of antibiotics; however, these drugs have to cross many barriers before they reach the infected implant. Modern micro/nanorobotics can deliver many drugs in situ, which is a new strategy to prevent infections in titanium-based implants. Therefore, based on the result presented in Figure 7, magnetic microrobots developed in this work were used to eradicate and remove biofilm from titanium mesh colonized with *S. aureus*. For this aim, small pieces (5 mm x 5 mm) of titanium mesh used for bone restoration were colonized with *S. aureus* biofilm. For this, the titanium meshes were inserted in LB medium inoculated with the bacteria and incubated for 24 h. Then the meshes were placed in an LB medium containing

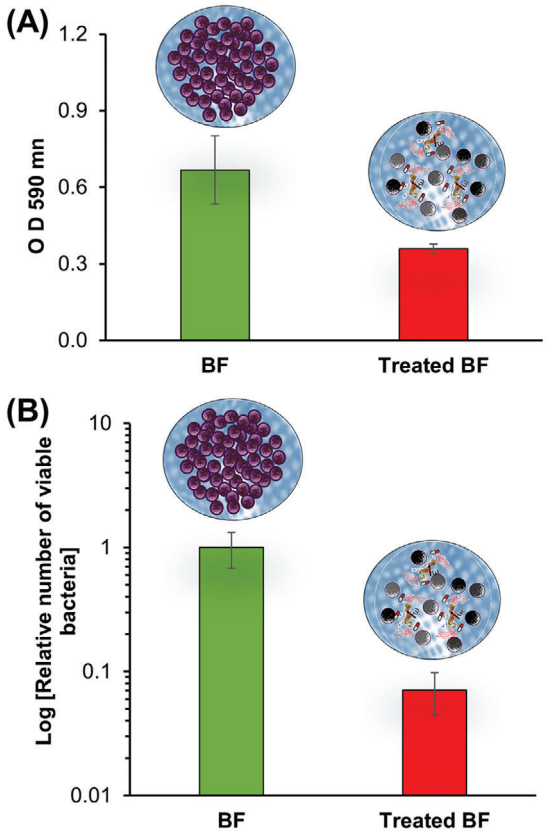

Figure 8. Removal and eradication of *S. aureus* biofilms colonizing mesh used for facial bone reconstruction. (A) Absorbance measurement at 590 nm of crystal violet staining of untreated and treated biofilms dissolved in DMSO. (B) Intact biofilm viability (control) is represented in the green column. Bacterial biofilm grown for 24 h and treated with Fe_3O_4-HNT/PEI@Amp is represented by the red column. Values are the average of three independent measurements and data are displayed as mean ± SD.

Fe_3O_4-HNT/PEI@Amp microrobots and magnetic actuation was applied for 60 min followed by 24 h incubation. After the incubation period, 60 min of magnetic actuation was applied. Biofilm-infected meshes without microrobots treatment were used as a control. Magnetic actuation occurred at 10 Hz, 5 mT, and under vortex motion mode. **Figure 8**A shows the biofilm adhesion to colonized meshes treated and untreated with magnetic microrobots. Moreover, bacterial biofilm viability decreased by two orders of magnitude in treated biofilm (red column) compared with intact biofilm (green column), representing 93% bacterial biofilm removal, see Figure 8B.

An in vitro cytotoxicity assay using resazurin in two cell lines (HeLa and MRC) was carried out to evaluate the biocompatibility of Fe_3O_4-HNT/PEI magnetic microrobots. The cells were exposed to different concentrations of magnetic robots for 24 h. Figure S4 (Supporting Information) shows the relative viability of cells exposed to different concentrations of microrobots. Clearly, cell viability was unchanged as evidenced by the metabolic activity observed, demonstrating that Fe_3O_4-HNT/PEI magnetic microrobots are biocompatible.

We also addressed the question of possible biodegradability of HNTs. There is no reported biological mechanism to degrade them; however, they can be removed from organisms by using macrophages. Moreover, the FDA considers HNTs as healthy and biocompatible material.[39]

We have explored previously HNT as the structural component of catalytic nanorobots.[40,41] However, in this work, the design, actuation, and applications are completely different. First, the reported HNT-based catalytic nanorobots are partially covered by a thin platinum film by sputtering and actuation is triggered by the decomposition of H_2O_2 (4%) on the Pt surface. However, such concentration of H_2O_2 is toxic and, thus, non-biocompatible. In this work, magnetic microrobots are prepared by bottom-up controlled assembly of halloysite nanotubes, Fe_3O_4 nanoparticles, polyethylenimine, and ampicillin. They are fuel-free-driven and their actuation is exclusively by the application of a transversal rotating magnetic field. Due to the magnetic actuation, these Fe_3O_4-HNT/PEI@Amp microrobots can be fully controlled and maneuvered, whereas in catalytic motors this is impossible. In addition, these microrobots exhibit multimodal motion as single robots as well as in swarms. They can transform from tumbling to spinning motion and vice-versa, and when in swarm mode, they can change their motion from vortex to ribbon and back again. In addition, reported catalytic micromotors have been used for water cleaning[40] and mercury detection,[41] and here the microrobots were used for biofilm removal. In summary, both our previous and current research demonstrates the great potential and versatility of HNTs used as microrobot skeletons, driven by different propulsion mechanisms, and for multiple applications.

3. Conclusion

In this work, we developed magnetic microrobots based on an HNT backbone and Fe_3O_4 magnetic actuator. These microrobots were coated with PEI to load ampicillin and obtain Fe_3O_4-HNT/PEI@Amp magnetic microrobots. Systematic chemical and morphological characterizations were performed to ensure their successful assembly. The role of the PEI layer was to load ampicillin and also to prevent the microrobots from disassembling. Moreover, PEI acts as β-lactam potentiator, helping the ampicillin to kill and remove efficiently up to 99% of bacteria from bacterial biofilm. Magnetic maneuvering demonstrated multimodal motion of single microrobots as well as their swarming behavior. Fe_3O_4-HNT/PEI@Amp magnetic microrobot swarms were able to switch from ribbon to vortex motion mode and back again. Furthermore, single Fe_3O_4-HNT/PEI@Amp magnetic microrobots were shown to transform their motion from tumbling to spinning and back to tumbling, and to avoid obstacles in their path. Finally, their vortex swarm behavior was used to penetrate the extracellular rigid matrix of *S. aureus* biofilm to achieve its almost total eradication and removal from infected titanium mesh used for bone restoration.

4. Experimental Section

Characterization of Fe_3O_4-HNT/PEI@Amp Magnetic Microrobots: Transmission electron microscope (TEM) EFTEM Jeol JEM-2200FS with an accelerating voltage 5 kV was used to obtain TEM images of each fabrication step of Fe_3O_4-HNT/PEI microrobots. A ZETASIZER PRO (Malvern) with a DTS1070 folded Capillary Zeta Cell (ANAMET s.r.o.) was used to obtain Z-potential values for each component of the Fe_3O_4-HNT/PEI microrobots. Thermogravimetric analysis was made using a TG-750 (Stanton Redcroft, England). The loading of ampicillin was quantified by mass spectrometry using electrospray ionization (ESI+) and orbital ion trap analysis (LTQ Orbitrap Velos, Thermo Fischer Scientific).

Fe_3O_4-HNT/PEI@Amp Magnetic Microrobot Fabrication: To synthetize Fe_3O_4-HNT/PEI@Amp magnetic microrobots, a solution of 1 mL of 1 mg/mL halloysite nanoclay (Sigma-Aldrich, Czech Republic) with 0.5 mg/mL of Fe_3O_4 nanopowder (Sigma-Aldrich, Czech Republic) was prepared and stirred overnight. After, the solution was rinsed twice with Milli-Q water using an external magnet. The obtained particles were suspended in a 2.5% PEI solution ($M_w = 7.5 \times 10^5$, Sigma-Aldrich, Czech Republic) and incubated overnight. The resulting solution was washed twice with water using an external magnet. Finally, Fe_3O_4-HNT/PEI solution was incubated overnight with ampicillin solution (5 mg/mL) and washed twice with water using an external magnet.

Staphylococcus Aureus Biofilm Preparation and Treatment with Fe_3O_4-HNT/PEI@Amp Magnetic Microrobots: *Staphylococcus aureus* strain was obtained from the collection of opportunistic pathogens at the Department of Biochemistry and Microbiology, UCT Prague, and then propagated on Luria–Bertani (LB) agar at 37°C and stored at 4°C. Biofilms were prepared by placing 2 mL of LB medium inoculated with the bacteria at optical density of 1 McFarland inside Petri dishes of 2 cm diameter and incubated for 24 h at 37°C. Small pieces of standard titanium mesh (Jeil Medical, Seoul, Republic of Korea) of 5 mm x 5 mm were colonized by placing them into 0.5 mL of the same LB medium inoculated with the bacteria. Then, supernatants of all samples were replaced with 1 mL (Petri dish) or 0.5 mL (mesh) of Fe_3O_4-HNT/PEI@Amp magnetic microrobots suspension (0.5 mg/mL) dispersed in LB medium and magnetic actuation was run for 60 min followed by incubation at 37°C for 24 h. Then, the magnetic actuation was run for 60 min. The supernatant was carefully removed and 0.5 mL (Petri dish) or 0.25 mL (mesh) of water was added. The remaining bacteria were removed from the Petri dish or mesh using an ultrasound bath and a viability test was performed. Magnetic actuation conditions: 10 Hz, 5 mT, and under vortex motion mode. For prepare intact biofilm, the experimental conditions were the same but without microrobots.

Small pieces of standard titanium mesh (Jeil Medical, Seoul, Republic of Korea) of 5 mm x 5 mm were colonized with *S. aureus*. Then, the titanium mesh was placed into an LB medium with Fe_3O_4-HNT/PEI@Amp magnetic microrobots. Next, magnetic actuation was applied for 1 h followed by 24 h incubation at 37°C. After, the titanium mesh was placed in water and the remaining bacteria were released using an ultrasound bath in order to evaluate their colony-forming ability.

Viability Evaluation of Bacteria: Suspensions of the remaining bacterial biofilm (treated and untreated with Fe_3O_4-HNT/PEI@Amp magnetic microrobots) were serially diluted in water. 15 µL droplets of each dilution were drop casted on an LB agar surface according to the Miles and Misra method, and incubated at 37°C overnight. Finally, colony-forming units were calculated from different dilutions.

Magnetic Actuation of Fe_3O_4-HNT/PEI@Amp Magnetic Microrobots: To evaluate the magnetic actuation of magnetic microrobots, video recordings were made using an Olympus inverted microscope with different objectives and with a Basler acA-1920-155 µm monochrome CMOS camera. In addition, a homemade 3D-printed six-coil system was attached to a microscope table to generate the transversal rotating magnetic field. Magnetic intensity in all experiments was 5 mT. Videos of the magnetic microrobots' performance and interaction with biofilms were recorded by placing them on a glass slide or in Petri dishes with biofilms, respectively.

Biofilm Visualization: *Staphylococcus aureus* biofilms treated with microrobots or washed only were stained with LIVE/DEAD staining and immediately visualized using spinning-disc confocal fluorescence microscopy at 488/525 nm (live) and 560/610 nm (dead).

Crystal Violet Staining: Biofilms were prepared and treated as described above, but the quantification was performed after drying the biofilm for 24 hours followed by staining with crystal violet solution and thorough washing with distilled water. After another 24 hours of drying,

the staining was documented by digital photography and the bound crystal violet was dissolved in DMSO and quantified as absorbance at 590 nm.

HeLa and MRC-5 Cells' Cultivation and Cytotoxic Assay: Cells were cultured in Minimum Essential Medium Eagle with 5% serum in a CO_2 chamber at 37°C. After seeding at 70% density, cells were treated with a range of Fe_3O_4-HNT/PEI@Amp magnetic microrobots concentrations and incubated for 24 hours. Finally, cell viability was determined using the resazurin assay.

Bacteria Characterization by SEM: Bacterial biofilms were prepared and treated as described above. The samples were then fixed in 4% formaldehyde for 20 minutes, gently washed with water, and dried. Finally, a gold thin layer of 5 nm is sputtered on the samples and SEM images were carried out using a field-emission scanning electron microscope (TESCAN MAIA 3 Tescan Ltd., Brno, Czech Republic) coupled with an energy-dispersive spectrometer (EDS) (Oxford Instruments, U.K.) and equipped with a field emission gun and cryogenic system PP3010 (Quorum Technologies Ltd., Sussex, U.K.).

Statistical Analysis: The bacterial viability scores shown in Figures 7,8 and Figures S1 and S2 (Supporting Information) are the averages of three independent measurements, and data are displayed as mean ± standard deviation (SD). For HeLa and MRC-5 cells, cytotoxicity evaluation values (Figure S4, Supporting Information), are the averages of three independent measurements and data are presented as mean ± SD. A two-tailed *t*-test with a confidence interval of 95% and significance level (α) of 0.05 was calculated to evaluate the statistical difference between control and treated biofilm. The data were analyzed using Microsoft Excel software.

Supporting Information

Supporting Information is available from the Wiley Online Library or from the author.

Acknowledgements

This work was supported by the project "Advanced Functional Nanorobots" (Reg. No. CZ.02.1.01/0.0/0.0/15_003/0000444 financed by the EFRR), Youth and Sports (Czech Republic).

Conflict of Interest

The authors declare no conflict of interest.

Data Availability Statement

The data that support the findings of this study are available from the corresponding author upon reasonable request.

Keywords

collective behavior, ribbons, swarms, vortices

Received: January 7, 2023
Revised: March 12, 2023
Published online: April 23, 2023

[1] H. Zhou, C. C. Mayorga-Martinez, S. Pané, L. Zhang, M. Pumera, *Chem. Rev.* **2021**, *121*, 4999.
[2] F. Soto, E. Karshalev, F. Zhang, B. E. Fernandez de Avila, A. Nourhani, J. Wang, *Chem. Rev.* **2022**, *122*, 5365.
[3] B. Jurado-Sánchez, A. Escarpa, *TrAC Trends Anal. Chem.* **2016**, *84*, 48.
[4] J. Gao, K. Yuan, L. Zhang, in *Field-Driven Micro and Nanorobots for Biology and Medicine* (Eds: Y. Sun, X. Wang, J. Yu) Springer, Cham, **2022**.
[5] M. Guix, C. C. Mayorga-Martinez, A. Merkoçi, *Chem. Rev.* **2014**, *114*, 6285.
[6] F. Zhang, Z. Li, Y. Duan, A. Abbas, R. Mundaca-Uribe, L. Yin, H. Luan, W. Gao, R. H. Fang, L. Zhang, J. Wang, *Sci. Robot* **2022**, *7*, eabo4160.
[7] B. Wang, S. Handschuh-Wang, J. Shen, X. Zhou, Z. Guo, W. Liu, M. Pumera, L. Zhang, *Adv. Mater.* **2022**, 2205732.
[8] M. Sun, K. F. Chan, Z. Zhang, L. Wang, Q. Wang, S. Yang, S. M. Chan, P. W. Y. Chiu, J. J. Y. Sung, L. Zhang, *Adv. Mater.* **2022**, *34*, 2201888.
[9] F. Zhang, J. Zhuang, Z. Li, H. Gong, B. Esteban-Fernández de Ávila, Y. Duan, Q. Zhang, J. Zhou, L. Yin, E. Karshalev, W. Gao, V. Nizet, R. H. Fang, L. Zhang, J. Wang, *Nat. Mater.* **2022**, *21*, 1324.
[10] Y. Dong, L. Wang, K. Yuan, F. Ji, J. Gao, Z. Zhang, X. Du, Y. Tian, Q. Wang, L. Zhang, *ACS Nano* **2021**, *15*, 5056.
[11] G. Hwang, A. J. Paula, E. E. Hunter, Y. Liu, A. Babeer, B. Karabucak, K. Stebe, V. Kumar, E. Steager, H. Koo, *Sci. Robot* **2019**, *4*, eaaw2388.
[12] C. C. Mayorga-Martinez, J. Zelenka, K. Klima, P. Mayorga-Burrezo, L. Hoang, T. Ruml, M. Pumera, *ACS Nano* **2022**, *16*, 8694.
[13] K. Yuan, B. Jurado-Sánchez, A. Escarpa, *Angew. Chem., Int. Ed.* **2021**, *60*, 4915.
[14] C. C. Mayorga-Martinez, J. Zelenka, J. Grmela, H. Michalkova, T. Ruml, J. Mareš, M. Pumera, *Adv. Sci.* **2021**, *8*, 2101301.
[15] V. Milosavljevic, L. Kosaristanova, K. Dolezelikova, V. Adam, M. Pumera, *Adv. Funct. Mater.* **2022**, *32*, 2112935.
[16] Y. Dong, L. Wang, Z. Zhang, F. Ji, T. K. F. Chan, H. Yang, C. P. L. Chan, Z. Yang, Z. Chen, W. T. Chang, J. Y. K. Chan, J. J. Y. Sung, L. Zhang, *Sci. Adv.* **2022**, *8*, eabq8573.
[17] C. C. Mayorga-Martinez, M. Castoralova, J. Zelenka, T. Ruml, M. Pumera, *Small* **2023**, *19*, 2205047.
[18] A. Algburi, N. Comito, D. Kashtanov, L. M. T. Dicks, M. L. Chikindas, *Appl. Environ. Microbiol.* **2017**, *83*, e02508.
[19] D. Sharma, L. Misba, A. U. Khan, *Antimicrob. Resist. Infect. Control* **2019**, *8*, 76.
[20] M. I. Hutchings, A. W. Truman, B. Wilkinson, *Curr. Opin. Microbiol.* **2019**, *51*, 72.
[21] G. R. Persson, S. Renvert, *Clin. Implant Dent. Relat. Res.* **2014**, *16*, 783.
[22] Y. Xie, S. Li, T. Zhang, C. Wang, X. Cai, *Int. J. Oral Sci.* **2020**, *12*, 37.
[23] M. Singh, A. S. Gill1, P. K. Deo, A. Agrawal, S. S. Sidhu, *J. Mater. Res.* **2022**, *37*, 2491.
[24] M. C. Hudson, W. K. Ramp, K. P. Frankenburg, *FEMS Microbiol. Lett.* **1999**, *173*, 279.
[25] M. Ussia, M. Urso, S. Kment, T. Fialova, K. Klima, K. Dolezelikova, M. Pumera, *Small* **2022**, *18*, 2200708.
[26] Z.-C. Zhao, Y. Zhou, G. Tan, J. Li, *Int. J. Ophthalmol.* **2018**, *11*, 1999.
[27] I. V. Ivanov, T. Mappes, P. Schaupp, C. Lappe, S. Wahl, *J. Biophotonics* **2018**, *11*, 201700377.
[28] J. D'Orazio, S. Jarrett, A. Amaro-Ortiz, T. Scott, *Int. J. Mol. Sci.* **2013**, *14*, 12222.
[29] M. A. Foxley, A. W. Friedline, J. M. Jensen, S. L. Nimmo, E. M. Scull, J. B. King, S. Strange, M. T. Xiao, B. E. Smith, K. J. Thomas III, D. T. Glatzhofer, R. H. Cichewicz, C. V. Rice, *J. Antibiot.* **2016**, *69*, 871.
[30] Y. Xie, D. Qian, D. Wu, X. Ma, *Chem. Eng. J.* **2011**, *168*, 959.
[31] J. Tully, R. Yendluri, Y. Lvov, *Biomacromolecules* **2016**, *17*, 615.
[32] X. Zhu, T. Uchikoshi, T. S. Suzuki, Y. Sakka, *J. Am. Ceram. Soc.* **2007**, *90*, 797.
[33] Z. Mokadem, S. Mekki, S. Saïdi-Besbes, G. Agusti, A. Elaissari, A. Derdour, *Arab J Chem* **2017**, *10*, 1039.
[34] V. Nairi, L. Medda, M. Monduzzi, A. Salis, *J. Colloid Interface Sci.* **2017**, *497*, 217.
[35] L. Thieme, M. Klinger-Strobel, A. Hartung, C. Stein, O. Makarewicz, M. W. Pletz, *J. Antimicrob. Chemother.* **2018**, *73*, 1553.

[36] L. L. Brunton, R. Hilal-Dandan, B. C. Knollmann, in *Goodman & Gilman's the Pharmacological Basis of Therapeutics*, McGraw Hill, New York, Unites States, **2017**.
[37] M. A. Foxley, S. N. Wright, A. K. Lam, A. W. Friedline, S. J. Strange, M. T. Xiao, E. L. Moen, C. V. Rice, *ACS Med. Chem. Lett.* **2017**, *8*, 1083.
[38] A. K. Lam, H. Panlilio, J. Pusavat, C. L. Wouters, E. L. Moen, A. J. Neel, C. V. Rice, *ACS Med. Chem. Lett.* **2020**, *11*, 473.
[39] I. N. H. M. Haneef, N. M. Shaffiar, Y. F. Buys, S. I. S. Shaharuddin , A. M. A. Hamid, K. Widiyati, *J. Biomed. Mater. Res.* **2022**, *110*, 2574.
[40] T. Maric, C. C. Mayorga-Martinez, B. Khezri, M. Z. M. Nasir, X. Chia, M. Pumera, *Adv. Funct. Mater.* **2018**, 1802762.
[41] T. Maric, C. C. Mayorga-Martinez, M. Z. M. Nasir, M. Pumera, *Adv. Mater. Techn.* **2019**, *4*, 1800502.